

# Real-space multifold degeneracy in graphene irradiated by twisted light

Suman Aich<sup>1</sup> and Babak Seradjeh<sup>1,2,3,\*</sup>

<sup>1</sup>*Department of Physics, Indiana University, Bloomington, Indiana 47405, USA*

<sup>2</sup>*Quantum Science and Engineering Center, Indiana University, Bloomington, Indiana 47405, USA*

<sup>3</sup>*IU Center for Spacetime Symmetries, Indiana University, Bloomington, Indiana 47405, USA*

We report the theoretical discovery of real-space multifold degenerate Floquet-Bloch states in monolayer graphene coherently driven by twisted circularly-polarized light. Using Floquet theory, we characterize the real-space structure of quasienergies and Floquet modes in terms of the orbital angular momentum and radial vortex profile of light. We obtain the effective real-space Floquet Hamiltonian and show it supports crossings of Floquet modes, especially at high-symmetry  $K$  and  $\Gamma$  points of graphene, at specific radial positions from the vortex center. At specific frequencies, the vortex bound states form a multifold degenerate structure in real-space. This structure is purely dynamically generated and controlled by the frequency and intensity of twisted light. We discuss the experimental feasibility of observing and employing the real-space multifold degeneracy for coherent optoelectronic quantum state engineering.

*Introduction.*—The proposal to generate quantum Hall states dynamically in irradiated graphene [1] opened a new research area [2–4] to harness the novel nonequilibrium dynamics of many-body systems, including the experimental realization of Floquet-Bloch bands in the solid state [5, 6] and synthetic systems [7], and theoretical advances in understanding the quantum thermodynamics of driven quantum systems [8–18] and Floquet topological phases in quantum materials [19–37]. The Floquet topological phases in graphene irradiated by circularly polarized light are characterized by a pair of topological invariants associated with quasienergy gaps at the Floquet zone center and boundary. As the frequency and amplitude of the light vary, the invariants change discontinuously at gap closings. Corresponding to these invariants are midgap modes bound to the edges of the sample that traverse the quasienergy gaps. Thus, spatial modulations of the light amplitude or frequency could be used to control the quasienergy gap structure and realize novel optically-tuned functionalities [38, 39].

A dramatic display of spatially modulated light is realized by optical beams carrying nonzero orbital angular momentum (OAM), the so-called twisted light, in which the field amplitude has a radial vortex profile and its phase winds around the propagation axis. Twisted linearly-polarized light can also break time-reversal symmetry and realize a Chern electronic insulator. However, despite the spatial variation, linear polarization does not induce variations of the local Chern marker [40–42].

In this Letter, we demonstrate that irradiating graphene with circularly polarized twisted light can realize multiple Floquet topological phases in the same sample. These phases form concentric rings around the light vortex center with a spatial profile determined by the amplitude and frequency of light. At the edges of the rings, the associated quasienergy gap at the Floquet zone center or boundary closes, resulting in Floquet edge modes. Moreover, we find that rings for different gap closings can be tuned to coincide at an infinite set of

frequencies, thus creating real-space multifold degeneracies of Floquet bound states. The size of these multifold degenerate rings can still be tuned by the optical field amplitude, opening a new avenue for optical quantum engineering and control of many-body electronic states. We provide analytical and numerical evidence for these multifold degeneracies and propose a protocol for quantum state control for Floquet bound states at high-symmetry points of graphene’s Brillouin zone.

*Setup and model.*—We consider graphene subject to coherent circularly-polarized light carrying orbital angular momentum at normal incidence, with vector potential components in the graphene plane coordinates  $x + iy = re^{i\phi}$  satisfying  $A_x + iA_y = A_0 f(r)e^{i(\Omega t + m\phi)}$ . Here  $A_0$  is the amplitude,  $\Omega$  is the frequency,  $f(r)$  is the spatial profile, and integer  $m$  is the OAM. Fig. 1 shows the schematics of the setup. We choose a particular form of  $f(r) = (r/\xi)^{|m|}e^{-(r/\xi)^2}$  for our numerical calculations, but we show in subsequent sections that our analytical

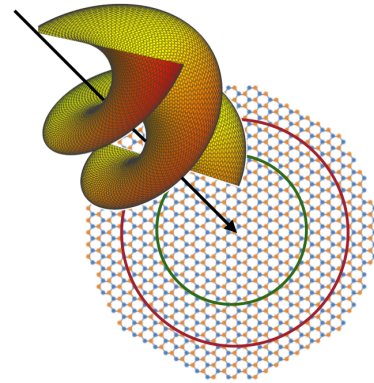


FIG. 1. Schematic of the setup with graphene irradiated by twisted light carrying orbital angular momentum. The vortex profile of twisted light and its angular phase winding allow for the creation of multiple Floquet topological phases and *in situ* optical quantum control of Floquet bound states.

results do not depend on the specific choice of  $f(r)$ . Here we assume  $\xi \gg a_0 = 0.142$  nm, the graphene lattice spacing, which allows us to treat the position  $\mathbf{r}$  as a parameter in our theory just as  $\Omega$  and  $A_0$ .

We calculate the Floquet eigenstates  $u_s^{(n)}(\mathbf{k}, \mathbf{r}, t)$  and the quasienergies  $\varepsilon_s^{(n)}(\mathbf{k}, \mathbf{r})$  satisfying the Floquet-Schrödinger equation  $H_F u_s^{(n)} = \varepsilon_s^{(n)} u_s^{(n)}$ , where the Floquet-Bloch Hamiltonian in the sublattice basis of graphene is given as ( $\hbar = 1$ ),

$$H_F(\mathbf{k}, \mathbf{r}, t) = \begin{pmatrix} -i\partial_t & -\gamma Z(\mathbf{k}, \mathbf{r}, t) \\ -\gamma Z^*(\mathbf{k}, \mathbf{r}, t) & -i\partial_t \end{pmatrix}, \quad (1)$$

Here,  $\gamma = 2.7$  eV is the nearest-neighbor hopping amplitude of graphene and the tight-binding structure factor  $Z(\mathbf{k}, \mathbf{r}, t) = \sum_{j=1}^3 e^{i[\mathbf{k}+(e/c)\mathbf{A}(\mathbf{r},t)]\cdot\mathbf{a}_j}$ , where the nearest-neighbor vectors  $\mathbf{a}_j = a_0(\cos\theta_j, \sin\theta_j)$ , with  $\theta_j = (2j-1)\pi/3$ . Keeping the lowest order in the Fourier expansion of  $Z(t)$ , we obtain [21, 43]

$$\varepsilon_{\pm}^{(n)}(\Gamma) = n\Omega \pm 3\gamma \mathcal{J}_0(\alpha f(r)), \quad (2)$$

$$u_{\pm}^{(n)}(\Gamma) = \frac{1}{\sqrt{2}} \begin{pmatrix} 1 \\ \mp 1 \end{pmatrix} e^{in\Omega t}, \quad (3)$$

at the  $\Gamma$  point, and

$$\varepsilon_{\pm}^{(n)}(\mathbf{K}) = \left(n + \frac{1}{2}\right)\Omega \pm \sqrt{\left(\frac{\Omega}{2}\right)^2 + [3\gamma \mathcal{J}_1(\alpha f(r))]^2}, \quad (4)$$

$$u_{\pm}^{(n)}(\mathbf{K}) = \frac{1}{\sqrt{2}} \begin{pmatrix} e^{i(\Omega t + m\phi)} u_{A,B} \\ u_{B,A} \end{pmatrix} e^{i(n\Omega t + \mathbf{K}\cdot\mathbf{r})}, \quad (5)$$

at the  $K$  point,  $\mathbf{K} = (0, -1)4\pi/3\sqrt{3}a_0$ . Here, the dimensionless amplitude  $\alpha = eA_0a_0/c$ ,  $\mathcal{J}_n$  is a Bessel function, and  $u_{A,B}$  are time-independent functions.

As in [21], the quasienergy spectrum contains various band crossings and avoided crossings between different Fourier modes; however, these crossings can now occur for a fixed value of frequency and light amplitude in the same irradiated graphene setup at different positions on the lattice.

*Effective Floquet Hamiltonian.*—To describe the real-space electronic structure near quasienergy band crossings, we project the Floquet-Bloch Hamiltonian onto the subspace of the two degenerate modes to obtain an effective Hamiltonian which has the general form,

$$\tilde{H}_F(\mathbf{k}, \mathbf{r}) = \mathbf{d}(\mathbf{k}, \mathbf{r}) \cdot \boldsymbol{\sigma} + \mu(r)\sigma_z, \quad (6)$$

where the Pauli matrices  $\boldsymbol{\sigma}$  act on the pseudospin subspace of the states  $u_{\pm}$  at the crossing, and  $\mu(r)$  is a dynamically generated mass term that depends only on the radial coordinate  $r$ . For the high-symmetry points like the  $\Gamma$  and  $K$ , this mass term vanishes at a critical radius  $r_c$  which results in a gap closing either at the Floquet

zone center,  $\varepsilon_0 = n\Omega$ , or at the Floquet zone boundary,  $\varepsilon_{\pi} = (2n+1)\Omega/2$ .

Using Eqs. (2) and (4), we find at the Floquet zone center, the crossings occur between  $\pm n_{\Gamma}$  Fourier modes at the  $\Gamma$  point and between  $n_K, -n_K - 1$  modes at the  $K$  point, where  $n_{\Gamma}, n_K > 0$  satisfy

$$|\mathcal{J}_0(\alpha f(r_c))| = n_{\Gamma} \frac{\Omega}{3\gamma}, \quad (7)$$

$$|\mathcal{J}_1(\alpha f(r_c))| = \sqrt{n_K(n_K+1)} \frac{\Omega}{3\gamma}. \quad (8)$$

Similarly, at the Floquet zone boundary, we find crossings between  $n_{\Gamma}, 1-n_{\Gamma}$  Fourier modes at the  $\Gamma$  point and  $\pm n_K$  at the  $K$ , with  $n_{\Gamma}, n_K > 0$  satisfying

$$|\mathcal{J}_0(\alpha f(r_c))| = \left(n_{\Gamma} - \frac{1}{2}\right) \frac{\Omega}{3\gamma}, \quad (9)$$

$$|\mathcal{J}_1(\alpha f(r_c))| = \sqrt{n_K^2 - \frac{1}{4}} \frac{\Omega}{3\gamma}. \quad (10)$$

Due to the structure of  $Z(t)$  at these high-symmetry points, avoided crossings are found when the Fourier modes are separated by a multiple of 3 [21]. Thus, degenerate states at the  $\Gamma$  and  $K$  points are found at the Floquet zone center when  $n_{\Gamma} \neq 0 \pmod{3}$  and  $n_K \neq 1 \pmod{3}$ , respectively. Conversely, at the Floquet zone edge, degenerate states are found when  $n_{\Gamma} \neq 2 \pmod{3}$  and  $n_K \neq 0 \pmod{3}$ . We also confirm [43] that, as with untwisted light [21], except for the  $\Gamma$ -point crossing at the Floquet zone boundary all other crossings are linear.

We find the Floquet eigenstates near band crossings by converting  $\mathbf{k}$  to the real-space operator  $-i\nabla_{\mathbf{r}}$  and solving the resulting differential equations. The details of our solution are presented in the Supplemental Material (SM) [43]. Here, we note that effective Hamiltonian commutes with a pseudo-OAM operator  $\hat{l}_z$  that combines the orbital and pseudospin angular momentum. Thus, we label the eigenstates of  $\tilde{H}_F$  with eigenvalue  $l$  of the pseudo-OAM operator,  $\chi_l(\mathbf{r})^T = (e^{il+\phi}w_+(r), e^{il-\phi}w_-(r))$ , where again  $\pm$  refer to the pseudospin subspace, and  $l_{\pm}$  are combinations of pseudo-OAM,  $l$ , and pseudospin eigenvalues. The complete Floquet eigenstate in the sublattice basis of graphene takes the form

$$\psi_l(\mathbf{r}, t) = e^{il+\phi}w_+(r)u_+(\mathbf{r}, t) + e^{il-\phi}w_-(r)u_-(\mathbf{r}, t), \quad (11)$$

where  $u_{\pm}$  are given by Eqs. (3) and (5) at the corresponding crossing.

We are particularly interested in bound-state solutions for which  $w_{\pm}$  are localized around  $r_c$ , where the mass term vanishes. These bound states form a ring of radius  $r_c$  separating two gapped regions in the graphene sheet. We present other analytical properties of these bound states in SM [43].

*Real-space multifold degeneracy.*—Remarkably, one can tune the ring of bound states for different crossings to

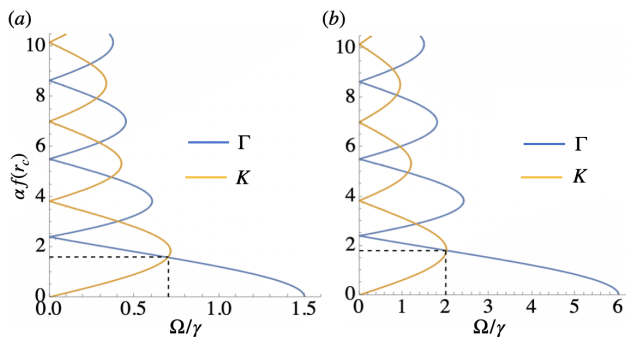


FIG. 2. Crossings and multifold degeneracy at  $\Gamma$  (blue) and  $K$  (orange) points at (a) Floquet zone center with  $n_\Gamma = n_K = 2$ , and (b) Floquet zone boundary with  $n_\Gamma = n_K = 1$ . The multifold degeneracies at (a)  $\alpha f(r_c) = 1.6$ ,  $\Omega/\gamma \approx 0.7$  and (b)  $\alpha f(r_c) = 1.8$ ,  $\Omega/\gamma \approx 2$  are indicated by dashed lines.

coincide at the same  $r_c$ . This realizes real-space multifold degeneracy between various crossings. Using Eqs. (7-10), we find that at the highest frequency, the critical radius for multifold degeneracy between the  $\Gamma$ - and  $K$ -point crossings satisfies  $\mathcal{F}_1(\alpha f(r_c)) = \sqrt{3/2}\mathcal{F}_0(\alpha f(r_c))$  with  $n_\Gamma = n_K = 2$  at the Floquet zone center, and  $\mathcal{F}_1(\alpha f(r_c)) = \sqrt{3}\mathcal{F}_0(\alpha f(r_c))$  with  $n_\Gamma = n_K = 1$  at the Floquet zone boundary. Solving these equations we obtain  $\alpha f(r_c) \approx 1.6$  and  $\Omega/\gamma \approx 0.7$  for multifold degeneracy at the Floquet zone center and  $\alpha f(r_c) \approx 1.8$  and  $\Omega/\gamma \approx 2$  at the Floquet zone boundary. Interestingly, since it is the value of  $\alpha f(r_c)$  that is fixed, the position of the multifold degenerate ring can be tuned by the amplitude  $\alpha$ .

In Fig. 2 we plot  $\alpha f(r_c)$  for  $\Gamma$ - and  $K$ -point crossings, with  $n_\Gamma = n_K = 2$  at Floquet zone center and  $n_\Gamma = n_K = 1$  at Floquet zone boundary, as a function of frequency. Multifold degeneracy is obtained at the intersection of these plots, giving rise to an infinite set of degenerate frequencies. There is in fact an infinite family of such sets, depending on the degenerate Fourier indices  $n_\Gamma$  and  $n_K$ . This offers a large space of parameters to obtain and tune multifold degenerate states.

Alternatively, real-space degeneracies may also obtain for one crossing at the Floquet zone center and the other at the Floquet zone boundary. When the former is a  $\Gamma$ -point crossing we find  $\mathcal{F}_1(\alpha f(r_c)) = (\sqrt{3}/2)\mathcal{F}_0(\alpha f(r_c))$  and  $n_\Gamma = n_K = 1$  at the highest frequency, so  $\alpha f(r_c) \approx 1.3$  and  $\Omega/\gamma \approx 1.8$ . When the former is a  $K$ -point crossing we find  $\mathcal{F}_1(\alpha f(r_c)) = 2\sqrt{6}\mathcal{F}_0(\alpha f(r_c))$  and  $n_\Gamma = n_K - 1 = 1$  at the highest frequency, so  $\alpha f(r_c) \approx 2.2$  and  $\Omega/\gamma \approx 0.7$ . In this case, the degenerate bound states are localized in the same region of space, but separated in crystal momentum and quasienergy.

We note that these real-space multifold degeneracies are distinguished from the higher-spin momentum-space multifold fermions protected by crystalline symmetries [44–47] by the fact that they occur at different

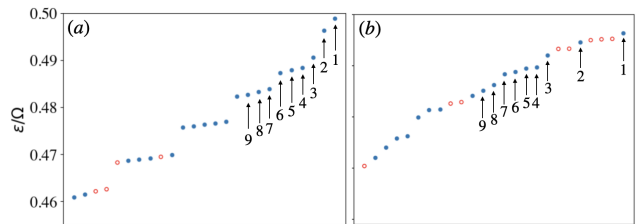


FIG. 3. Quasienergies near Floquet zone boundary for (a)  $\alpha = 3$ ,  $m = 1$ ,  $\xi = 100a_0$ ,  $\Omega/\gamma = 5.8$ , and (b)  $\alpha = 22.3$ ,  $m = 1$ ,  $\xi = 100a_0$  nm, and  $\Omega/\gamma = 1$ . Analytically, we expect a single  $\Gamma$ -point crossings for (a) at  $r_c = 1.76$  nm and a single  $K$ -point crossing for (b) at  $r_c = 2.04$  nm. The blue dots and red circles represent bulk and edge bound states respectively. The numbered bulk edge states are presented in Fig. 4.

momenta in the Brillouin zone and are localized in space.

*Numerical results.*—We numerically diagonalize the Floquet time-evolution operator using the full tight-binding Hamiltonian in real space and obtain the Floquet spectrum. We take a graphene sample with a disk geometry of radius  $3$  nm  $\approx 21a_0$ . The twisted light is implemented as  $f(r) = (r/\xi)^{|m|}e^{-(r/\xi)^2}$  with  $r$  measured from the center of the disk. We take a large value of  $\xi = 100a_0$  to explore the Floquet states within the light vortex core. The values of other parameters are chosen so that, based on our analytical expressions, we expect to obtain a single band crossing at either the  $\Gamma$  point or  $K$  point at the Floquet zone boundary within the disk. Note that these values are not representative for experiments, rather they are chosen to allow efficient numerical simulations for relatively small system sizes [48].

Our results are shown in Figs. 3 and 4. We find that the states near the Floquet zone boundary shown in Fig. 3 are indeed localized either within the disk (shown by blue dots) or near its edges (red circles). This is so because the two regions separated at  $r_c$  are in different Floquet topological phases.

We present the wavefunctions of several localized states within the sample in Fig. 4. The real-space probability distributions  $|\psi(\mathbf{r})|^2$  shown in Fig. 4(a) and Fig. 4(d) clearly show localization near the expected values of  $r_c = 1.76$  nm and  $r_c = 2.04$  nm (shown as red circles) for the  $\Gamma$ - and  $K$ -point crossings, respectively. They also show an intricate orbital structure within the sample.

In order to test the type of band crossing producing the bound states, we perform a numerical Fourier transform of the wavefunctions separately for each sublattice to obtain  $\psi_{A/B}(\mathbf{k}) = \sum_{\mathbf{r} \in A/B} e^{-i\mathbf{k} \cdot \mathbf{r}} \psi(\mathbf{r})$ . The probability distributions  $|\psi_A(\mathbf{k})|^2$  and  $|\psi_B(\mathbf{k})|^2$  are shown in Fig. 4(b)-(c) and Fig. 4(e)-(f). They show clear localization around  $\Gamma$  and  $K$  points, respectively. Thus, our numerics confirm our analytical findings and provide additional information about the orbital structure of the bound states.

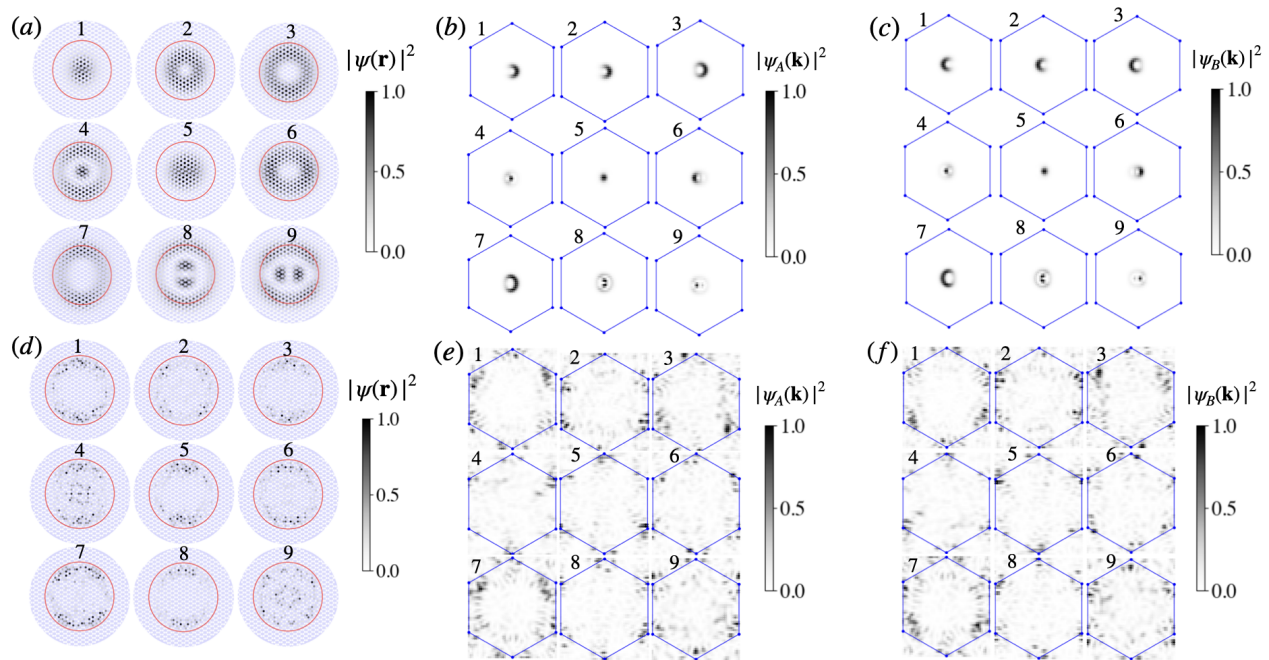


FIG. 4. Probability distributions in real space (a and d) and momentum space (b, c and e, f) for states numbered 1-9 in Fig. 3(a) (top row) and Fig. 3(b) (bottom row). The red circles show values (a)  $r_c = 1.76$  nm and (d)  $r_c = 2.04$  nm calculated analytically for  $\Gamma$ - and  $K$ -point crossings at the Floquet zone boundary, respectively. The blue hexagon in (b-c) and (e-f) mark the graphene Brillouin zone.

*Discussion.*—The main property of the twisted light we have used so far is the vortex profile  $f(r)$ , which creates a spatially variable amplitude  $\alpha f(r)$  and, therefore, the possibility of concurrent realizations of multiple Floquet topological phases in the same sample. The angular winding of the light amplitude only appears in the wavefunctions through the Floquet states, Eqs. (3) and (5), and the pseud-OAM eigenvalues in Eq. (11). It is natural to ask if this angular dependence manifests itself in a more direct way. We answer this question in the affirmative by investigating a way to control the quantum states of multifold degenerate bound states associated with  $\Gamma$ - and  $K$ -point crossings.

In particular, we propose to manipulate quantum superpositions of the  $\Gamma$ - and  $K$ -point multifold bound states through a localized real-space scattering potential  $V(\mathbf{r})$  that connects  $\Gamma$  to  $K$ . Such a potential must have some variation between the two sublattices with wave vector  $\mathbf{K}$ , which can naturally exist at the edges of the system or may be created artificially. By tuning the light amplitude  $\alpha$ , we can tune  $r_c$  for multifold degenerate states to coincide with the region where  $V(\mathbf{r}) \neq 0$ . As we show in SM [43], due to the differences in the linear vs. quadratic band crossings, for such a potential to have nonzero matrix elements between  $\Gamma$ - and  $K$ -point degenerate states, the light OAM must take values  $m = \pm 2$  at Floquet zone center and  $m = \pm 1$  at Floquet zone boundary.

Assuming the scattering potential has a primary wave vector  $\mathbf{K}$ , the dominant scattering process connects  $\Gamma$  not

only to the  $K$ -point bound states, but also to the  $K'$ -point bound states at the opposite valley. The multifold degeneracy conditions and OAM values for  $\Gamma \leftrightarrow K'$  and  $\Gamma \leftrightarrow K$  transitions are the same. However, the matrix elements for the two transitions can be different from each other and may be switched by the helicity of the circular polarization as well as the sign of  $m$ .

Therefore, employing OAM offers the possibility to engineer and control two-level systems from multifold degeneracies at the Floquet zone center and boundary. In the ideal situation of nonvanishing couplings  $b$  and  $b'$ , respectively, between  $\Gamma$  and  $K$ ,  $\Gamma$  and  $K'$ , the two levels are formed from the  $\Gamma$ -point bound state and a superposition of  $K$ - and  $K'$ -point bound states weighted by  $b$  and  $b'$ . Quantum operations can proceed by tuning  $r_c$  via the light amplitude  $\alpha$ : the two levels are stationary as long as  $r_c$  does not overlap with  $V(\mathbf{r}) \neq 0$ , while a rotation between the two levels is achieved by tuning  $r_c$  to overlap  $V(\mathbf{r}) \neq 0$  for a time  $t$ , with a precession frequency  $\sim \sqrt{b^2 + b'^2}$ . Some details of the calculations for the quantum state manipulation process described here are presented in the SM.

For electric field amplitude  $2 \times 10^8$  V/m in the lab, corresponding to intensities  $10^9$  W/cm<sup>2</sup>, we obtain  $\alpha \approx 10^{-2}(\Omega/\gamma)^{-1}$ . So, for  $\Omega/\gamma \approx 0.1$ , we can achieve  $\alpha \approx 0.1$ . Since the vortex profile  $f(r) \lesssim 1$ , we must have  $\alpha \gtrsim \alpha f(r_c)$  to realize multifold degeneracies. For  $f(r_c) \lesssim 1$  we find  $r_c \sim \xi \sim c/\Omega \approx 5 \times 10^3 a_0$ . Thus, micron-sized samples of graphene can accommodate multifold degeneracies

near their edges. One may utilize higher Fourier modes to enlarge the experimental feasibility of parameters for multifold degeneracy. For example, fixing  $n_K = 2$  and varying  $n_\Gamma > 2$  (and  $\neq 0 \pmod{3}$ ) we obtain the highest-frequency multifold degeneracy for  $\alpha f(r_c) \approx 2\sqrt{6}n_\Gamma^{-1}$  and  $\Omega/\gamma \approx 3n_\Gamma^{-1}$  at the Floquet zone center. Similarly, fixing  $n_K = 1$  and varying  $n_\Gamma > 2$  (and  $\neq 2 \pmod{3}$ ) we obtain the highest-frequency multifold degeneracy for  $\alpha f(r_c) \approx 2\sqrt{3}(2n_\Gamma - 1)^{-1}$  and  $\Omega/\gamma \approx 6(2n_\Gamma - 1)^{-1}$  at the Floquet zone boundary. For example, going to Fourier mode  $n_\Gamma = 10$ , we have  $\alpha f(r_c) \approx 0.5$  at Floquet zone center and  $\alpha f(r_c) \approx 0.2$  at Floquet zone boundary with  $\Omega/\gamma \approx 0.3$  in the infrared.

We have studied the interaction of twisted circularly-polarized light with graphene and shown, both analytically and numerically, that multiple Floquet topological phases can be realized in the same sample. At certain frequencies, real-space multifold degenerate states become possible and may be tuned by light amplitude, thus creating a possible route for *in situ* optical quantum state control of light-matter bound states. An interesting possibility to explore is using additional hamornics [39] of twisted light to control the quantum states of the valleys, which may be operated with graphene leads.

This work is supported in part by the College of Arts and Sciences and the Institute for Advanced Study at Indiana University.

---

\* babaks@indiana.edu.

- [1] T. Oka and H. Aoki, *Photovoltaic Hall effect in graphene*, Phys. Rev. B **79**, 081406 (2009).
- [2] T. Oka and S. Kitamura, *Floquet Engineering of Quantum Materials*, Annual Review of Condensed Matter Physics **10**, 387 (2019).
- [3] M. S. Rudner and N. H. Lindner, *Band structure engineering and non-equilibrium dynamics in Floquet topological insulators*, Nature Reviews Physics **2**, 229 (2020).
- [4] A. de la Torre, D. M. Kennes, M. Claassen, S. Gerber, J. W. McIver, and M. A. Sentef, *Colloquium: Nonthermal pathways to ultrafast control in quantum materials*, Rev. Mod. Phys. **93**, 041002 (2021).
- [5] Y. H. Wang, H. Steinberg, P. Jarillo-Herrero, and N. Gedik, *Observation of Floquet-Bloch States on the Surface of a Topological Insulator*, Science **342**, 453 (2013).
- [6] J. W. McIver, B. Schulte, F.-U. Stein, T. Matsuyama, G. Jotzu, G. Meier, and A. Cavalleri, *Light-induced anomalous Hall effect in graphene*, Nature Physics **16**, 38 (2019).
- [7] M. C. Rechtsman, J. M. Zeuner, Y. Plotnik, Y. Lumer, D. Podolsky, F. Dreisow, S. Nolte, M. Segev, and A. Szameit, *Photonic Floquet topological insulators*, Nature **496**, 196 (2013).
- [8] P. Ponte, A. Chandran, Z. Papić, and D. A. Abanin, *Periodically driven ergodic and many-body localized quantum systems*, Annals of Physics **353**, 196 (2015).
- [9] P. Ponte, Z. Papić, F. m. c. Huveneers, and D. A. Abanin, *Many-Body Localization in Periodically Driven Systems*, Phys. Rev. Lett. **114**, 140401 (2015).
- [10] D. A. Abanin, W. D. Roeck, and F. Huveneers, *Theory of many-body localization in periodically driven systems*, Annals of Physics **372**, 1 (2016).
- [11] V. Khemani, A. Lazarides, R. Moessner, and S. L. Sondhi, *Phase Structure of Driven Quantum Systems*, Phys. Rev. Lett. **116**, 250401 (2016).
- [12] D. V. Else and C. Nayak, *Classification of topological phases in periodically driven interacting systems*, Physical Review B **93**, 201103 (2016).
- [13] S. D. Geraedts, R. Nandkishore, and N. Regnault, *Many-body localization and thermalization: Insights from the entanglement spectrum*, Physical Review B **93**, 174202 (2016).
- [14] P. Bordia, H. Lüschen, U. Schneider, M. Knap, and I. Bloch, *Periodically driving a many-body localized quantum system*, Nature Physics **13**, 460 (2017).
- [15] D. V. Else, B. Bauer, and C. Nayak, *Floquet Time Crystals*, Phys. Rev. Lett. **117**, 090402 (2016).
- [16] N. Y. Yao, A. C. Potter, I.-D. Potirniche, and A. Vishwanath, *Discrete Time Crystals: Rigidity, Criticality, and Realizations*, Physical Review Letters **118**, 030401 (2017).
- [17] J. Zhang, P. W. Hess, A. Kyprianidis, P. Becker, A. Lee, J. Smith, G. Pagano, I.-D. Potirniche, A. C. Potter, A. Vishwanath, N. Y. Yao, and C. Monroe, *Observation of a discrete time crystal*, Nature **543**, 217 (2017).
- [18] V. Khemani, C. W. von Keyserlingk, and S. L. Sondhi, *Defining time crystals via representation theory*, Phys. Rev. B **96**, 115127 (2017).
- [19] N. H. Lindner, G. Refael, and V. Galitski, *Floquet topological insulator in semiconductor quantum wells*, Nature Physics **7**, 490 (2011).
- [20] J. Cayssol, B. Dóra, F. Simon, and R. Moessner, *Floquet topological insulators*, physica status solidi (RRL) – Rapid Research Letters **7**, 101 (2013).
- [21] A. Kundu, H. A. Fertig, and B. Seradjeh, *Effective Theory of Floquet Topological Transitions*, Phys. Rev. Lett. **113**, 236803 (2014).
- [22] G. Usaj, P. M. Perez-Piskunow, L. E. F. Foa Torres, and C. A. Balseiro, *Irradiated graphene as a tunable Floquet topological insulator*, Phys. Rev. B **90**, 115423 (2014).
- [23] M. Rodriguez-Vega, A. Kumar, and B. Seradjeh, *Higher-order Floquet topological phases with corner and bulk bound states*, Phys. Rev. B **100**, 085138 (2019).
- [24] B. Huang and W. V. Liu, *Floquet Higher-Order Topological Insulators with Anomalous Dynamical Polarization*, Phys. Rev. Lett. **124**, 216601 (2020).
- [25] A. K. Ghosh, G. C. Paul, and A. Saha, *Higher order topological insulator via periodic driving*, Phys. Rev. B **101**, 235403 (2020).
- [26] T. Nag, V. Juričić, and B. Roy, *Hierarchy of higher-order Floquet topological phases in three dimensions*, Phys. Rev. B **103**, 115308 (2021).
- [27] W. Zhu, Y. D. Chong, and J. Gong, *Floquet higher-order topological insulator in a periodically driven bipartite lattice*, Phys. Rev. B **103**, L041402 (2021).
- [28] L. Zhou, *Floquet Second-Order Topological Phases in Momentum Space*, Nanomaterials **11**, 1170 (2021).
- [29] R. W. Bomantara, G. N. Raghava, L. Zhou, and J. Gong, *Floquet topological semimetal phases of an extended kicked Harper model*, Phys. Rev. E **93**, 022209 (2016).
- [30] K. W. Kim, H. Kwon, and K. Park, *Floquet topological*

- semimetal with a helical nodal line in 2+1 dimensions*, Phys. Rev. B **99**, 115136 (2019).
- [31] P. Wang, Q.-f. Sun, and X. C. Xie, *Transport properties of Floquet topological superconductors at the transition from the topological phase to the Anderson localized phase*, Phys. Rev. B **90**, 155407 (2014).
- [32] B. Bauer, T. Pereg-Barnea, T. Karzig, M.-T. Rieder, G. Refael, E. Berg, and Y. Oreg, *Topologically protected braiding in a single wire using Floquet Majorana modes*, Phys. Rev. B **100**, 041102 (2019).
- [33] T. Čadež, R. Mondaini, and P. D. Sacramento, *Edge and bulk localization of Floquet topological superconductors*, Phys. Rev. B **99**, 014301 (2019).
- [34] Y. Peng, *Floquet higher-order topological insulators and superconductors with space-time symmetries*, Phys. Rev. Res. **2**, 013124 (2020).
- [35] L. Zhou, *Non-Hermitian Floquet topological superconductors with multiple Majorana edge modes*, Phys. Rev. B **101**, 014306 (2020).
- [36] D. Mondal, A. K. Ghosh, T. Nag, and A. Saha, *Topological characterization and stability of Floquet Majorana modes in Rashba nanowires*, Phys. Rev. B **107**, 035427 (2023).
- [37] H. Wu, S. Wu, and L. Zhou, *Floquet topological superconductors with many Majorana edge modes: topological invariants, entanglement spectrum and bulk-edge correspondence*, New Journal of Physics **25**, 083042 (2023).
- [38] Y. T. Katan and D. Podolsky, *Modulated Floquet Topological Insulators*, Phys. Rev. Lett. **110**, 016802 (2013).
- [39] A. Kundu, H. A. Fertig, and B. Seradjeh, *Floquet-Engineered Valleytronics in Dirac Systems*, Phys. Rev. Lett. **116**, 016802 (2016).
- [40] R. Bianco and R. Resta, *Mapping topological order in coordinate space*, Phys. Rev. B **84**, 241106 (2011).
- [41] H. Kim, H. Deghani, I. Ahmadabadi, I. Martin, and M. Hafezi, *Floquet vortex states induced by light carrying an orbital angular momentum*, Phys. Rev. B **105**, L081301 (2022).
- [42] U. Bhattacharya, S. Chaudhary, T. Grass, A. S. Johnson, S. Wall, and M. Lewenstein, *Fermionic Chern insulator from twisted light with linear polarization*, Phys. Rev. B **105**, L081406 (2022).
- [43] Supplemental Material, where we present the details of our calculation for the Floquet spectra, effective Hamiltonians near  $\Gamma$ - and  $K$ -point band crossings at Floquet zone center and boundary, analytical results for Floquet bound states, selection rules for  $\Gamma \leftrightarrow K$  transitions, and the two-level quantum control protocol using these transitions.
- [44] F. Flicker, F. de Juan, B. Bradlyn, T. Morimoto, M. G. Vergniory, and A. G. Grushin, *Chiral optical response of multifold fermions*, Phys. Rev. B **98**, 155145 (2018).
- [45] N. B. M. Schröter, D. Pei, M. G. Vergniory, Y. Sun, K. Manna, F. de Juan, J. A. Krieger, V. Süss, M. Schmidt, P. Dudin, B. Bradlyn, T. K. Kim, T. Schmitt, C. Cacho, C. Felser, V. N. Strocov, and Y. Chen, *Chiral topological semimetal with multifold band crossings and long Fermi arcs*, Nature Physics **15**, 759 (2019).
- [46] M.-Á. Sánchez-Martínez, F. de Juan, and A. G. Grushin, *Linear optical conductivity of chiral multifold fermions*, Physical Review B **99**, 155145 (2019).
- [47] B. Xu, Z. Fang, M.-Á. Sánchez-Martínez, J. W. F. Venderbos, Z. Ni, T. Qiu, K. Manna, K. Wang, J. Paglione, C. Bernhard, C. Felser, E. J. Mele, A. G. Grushin, A. M. Rappe, and L. Wu, *Optical signatures of multifold fermions in the chiral topological semimetal CoSi*, Proceedings of the National Academy of Sciences **117**, 27104 (2020).
- [48] Code available at Zenodo doi:10.5072/zenodo.10003885, <https://sandbox.zenodo.org/records/10003885>.

# Supplemental material for “Real-space multifold degeneracy in graphene irradiated by twisted light”

Suman Aich,<sup>1</sup> Babak Seradjeh,<sup>1,2,3,\*</sup> Suman Aich,<sup>1</sup> and Babak Seradjeh<sup>1,2,3</sup>

<sup>1</sup>*Department of Physics, Indiana University, Bloomington, Indiana 47405, USA*

<sup>2</sup>*Quantum Science and Engineering Center, Indiana University, Bloomington, Indiana 47405, USA*

<sup>3</sup>*IU Center for Spacetime Symmetries, Indiana University, Bloomington, Indiana 47405, USA*

We present the details of our calculation for the Floquet spectra, effective Hamiltonians near  $\Gamma$ - and  $K$ -point band crossings at Floquet zone center and boundary, analytical results for Floquet bound states, selection rules for  $\Gamma \leftrightarrow K$  transitions, and the two-level quantum control protocol using these transitions.

## FOURIER COMPONENTS OF THE STRUCTURE FACTOR

The tight-binding structure factor is given by

$$Z(\mathbf{k}, \mathbf{r}, t) = \sum_{j=1}^3 e^{i[\mathbf{k} + (e/c)\mathbf{A}(r, \phi, t)] \cdot \mathbf{a}_j}, \quad (\text{S1})$$

where  $\mathbf{a}_j = a_0(\cos \theta_j, \sin \theta_j)$ , with  $\theta_j = (2j - 1)\pi/3$ , being the primitive vectors for the honeycomb lattice in graphene ( $a_0 = 0.142$  nm). It can be decomposed into its Fourier components  $Z(\mathbf{k}, \mathbf{r}, t) = \sum_n Z_n(\mathbf{k}, \mathbf{r}) e^{-in\Omega t}$ , where

$$Z_n(\mathbf{k}, \mathbf{r}) = i^n \mathcal{J}_n(\alpha f(r)) \left[ (-1)^n e^{-ik_x a_0} + 2e^{ik_x a_0/2} \cos\left(\frac{n\pi}{3} + \frac{\sqrt{3}}{2} k_y a_0\right) \right] e^{-inm\phi}, \quad (\text{S2})$$

and  $\mathcal{J}_n$  is the  $n^{\text{th}}$  order Bessel function and  $\alpha = eA_0 a_0/c$  is the dimensionless amplitude.

## EFFECTIVE HAMILTONIANS AT THE $\Gamma$ AND $K$ - POINTS

### Floquet zone center

We have  $\mp n_\Gamma$  modes that are degenerate at  $\Gamma$  and  $n_K, -n_K - 1$  modes degenerate at  $K$  with  $n_\Gamma, n_K > 0$  ( $n_\Gamma \neq 0 \pmod{3}$  and  $n_K \neq 1 \pmod{3}$ ). The degenerate Floquet eigenstates are  $\frac{1}{\sqrt{2}} \begin{pmatrix} 1 \\ \mp 1 \end{pmatrix} e^{\mp in_\Gamma \Omega t}$  for  $\Gamma$  and  $\frac{1}{\sqrt{2}} \begin{pmatrix} e^{i(\Omega t + m\phi)} u_A \\ u_B \end{pmatrix} e^{i(n_K \Omega t + \mathbf{K} \cdot \mathbf{r})}$  and  $\frac{1}{\sqrt{2}} \begin{pmatrix} e^{i(\Omega t + m\phi)} u_B \\ u_A \end{pmatrix} e^{-i((n_K + 1)\Omega t - \mathbf{K} \cdot \mathbf{r})}$  for  $K$ . Thus, in the degenerate subspace, the matrix elements of the effective Hamiltonian at  $\Gamma$  are

$$(\tilde{H}_F)_{11}^{\Gamma(0)} = -(\tilde{H}_F)_{22}^{\Gamma(0)} = -n_\Gamma \Omega + 3\gamma \mathcal{J}_0(\alpha f(r)) \left( 1 - \frac{k^2 a_0^2}{4} \right), \quad (\text{S3})$$

$$(\tilde{H}_F)_{12}^{\Gamma(0)} = i(-1)^{n_\Gamma} \frac{3\gamma}{2} \mathcal{J}_{2n_\Gamma}(\alpha f(r)) [k_x + i(-1)^{n_\Gamma \pmod{3}} k_y] a_0 e^{-2in_\Gamma m\phi}, \quad (\text{S4})$$

and at  $K$  are

$$(\tilde{H}_F)_{11}^{K(0)} = -(\tilde{H}_F)_{22}^{K(0)} = \frac{1}{\eta^2 + 1} \left[ ((n_K + 1)\eta^2 + n_K) \Omega + 6\gamma \eta \mathcal{J}_1(\alpha f(r)) \left( 1 - \frac{k^2 a_0^2}{4} \right) \right], \quad (\text{S5})$$

$$(\tilde{H}_F)_{12}^{K(0)} = i(-1)^{(n_K + 1)} \frac{3\gamma}{2(\eta^2 + 1)} \mathcal{J}_{2n_K}(\alpha f(r)) (k_x - i\beta k_y) a_0 e^{i(2n_K + 1)m\phi}, \quad (\text{S6})$$

where  $\beta = +1$  for  $n_K = 0 \pmod{3}$  and  $\beta = -1$  for  $n_K = 2 \pmod{3}$ , respectively. We have also introduced

$$\eta(r) = -i \frac{u_A}{u_B} = \frac{\frac{\Omega}{2} - \sqrt{\left(\frac{\Omega}{2}\right)^2 + [3\gamma \mathcal{J}_1(\alpha f(r))]^2}}{3\gamma \mathcal{J}_1(\alpha f(r))}. \quad (\text{S7})$$

Due to the particular angular structure of  $\tilde{H}_F^{\Gamma(0)}$  and  $\tilde{H}_F^{K(0)}$ , we have  $[\tilde{H}_F^{\Gamma(0)}, \hat{l}^{\Gamma(0)}] = 0$  and  $[\tilde{H}_F^{K(0)}, \hat{l}^{K(0)}] = 0$ , where  $\hat{l}^{\Gamma(0)}$  and  $\hat{l}^{K(0)}$  are the respective psuedo-OAM operators given by

$$\hat{l}^{\Gamma(0)} = -i\partial_\phi + \left( n_\Gamma m - \frac{(-1)^{n_\Gamma \bmod 3}}{2} \right) \sigma_z, \quad (\text{S8})$$

$$\hat{l}^{K(0)} = -i\partial_\phi - \left[ \frac{(2n_K + 1)m - \beta}{2} \right] \sigma_z. \quad (\text{S9})$$

Correspondingly, the eigenvalues of the pseudo-OAM operators are

$$l_\pm^{\Gamma(0)} = l \mp \left( n_\Gamma m - \frac{(-1)^{n_\Gamma \bmod 3}}{2} \right), \quad (\text{S10})$$

$$l_\pm^{K(0)} = l \pm \left[ \frac{(2n_K + 1)m - \beta}{2} \right], \quad (\text{S11})$$

for  $\Gamma$  and  $K$  respectively. Thus, from the effective Hamiltonians we can see that there is a linear band crossing at both  $\Gamma$  and  $K$  points. The complete Floquet eigenstate for zero quasi-energy at the  $\Gamma$  point can be written as,

$$\psi_l^{\Gamma(0)}(\mathbf{r}, t) = e^{il_+^{\Gamma(0)}\phi} w_+^{\Gamma(0)}(r) u_+^{(-n_\Gamma)}(\Gamma, \mathbf{r}, t) + e^{il_-^{\Gamma(0)}\phi} w_-^{\Gamma(0)}(r) u_-^{(n_\Gamma)}(\Gamma, \mathbf{r}, t). \quad (\text{S12})$$

Similarly, for the  $K$  point

$$\psi_l^{K(0)}(\mathbf{r}, t) = e^{il_+^{K(0)}\phi} w_+^{K(0)}(r) u_+^{(n_K)}(K, \mathbf{r}, t) + e^{il_-^{K(0)}\phi} w_-^{K(0)}(r) u_-^{(-n_K-1)}(K, \mathbf{r}, t). \quad (\text{S13})$$

### Floquet zone boundary

We have  $1 - n_\Gamma, n_\Gamma$  modes that are degenerate at  $\Gamma$  and  $\pm n_K$  modes degenerate at  $K$  with  $n_\Gamma, n_K > 0$  ( $n_\Gamma \neq 2 \bmod 3$  and  $n_K \neq 0 \bmod 3$ ). The degenerate Floquet eigenstates are  $\frac{1}{\sqrt{2}} \begin{pmatrix} 1 \\ -1 \end{pmatrix} e^{-i(n_\Gamma-1)\Omega t}$  and  $\frac{1}{\sqrt{2}} \begin{pmatrix} 1 \\ 1 \end{pmatrix} e^{in_\Gamma\Omega t}$  for  $\Gamma$  and  $\frac{1}{\sqrt{2}} \begin{pmatrix} e^{i(\Omega t + m\phi)} u_{A,B} \\ u_{B,A} \end{pmatrix} e^{\pm i(n_K\Omega t \pm \mathbf{K}\cdot\mathbf{r})}$  for  $K$ . Thus, in the degenerate subspace, the matrix elements of the effective Hamiltonian at  $\Gamma$  are

$$(\tilde{H}_F)_{11}^{\Gamma(\pi)} = \frac{\Omega}{2} + \left[ - \left( n_\Gamma - \frac{1}{2} \right) \Omega + 3\gamma \mathcal{J}_0(\alpha f(r)) \left( 1 - \frac{a_0^2}{4} k^2 \right) \right], \quad (\text{S14})$$

$$(\tilde{H}_F)_{12}^{\Gamma(\pi)} = i(-1)^{n_\Gamma} \frac{3\gamma}{8} \mathcal{J}_{2n_\Gamma-1}(\alpha f(r)) (k_x + i(-1)^{n_\Gamma \bmod 3} k_y)^2 a_0^2 e^{-i(2n_\Gamma-1)m\phi}, \quad (\text{S15})$$

$$(\tilde{H}_F)_{22}^{\Gamma(\pi)} = \frac{\Omega}{2} - \left[ - \left( n_\Gamma - \frac{1}{2} \right) \Omega + 3\gamma \mathcal{J}_0(\alpha f(r)) \left( 1 - \frac{a_0^2}{4} k^2 \right) \right], \quad (\text{S16})$$

and at  $K$  are

$$(\tilde{H}_F)_{11}^{K(\pi)} = \frac{\Omega}{2} + \frac{1}{\eta^2 + 1} \left[ \left\{ \left( n_K + \frac{1}{2} \right) \eta^2 + \left( n_K - \frac{1}{2} \right) \right\} \Omega + 6\gamma\eta \mathcal{J}_1(\alpha f(r)) \left( 1 - \frac{k^2 a_0^2}{4} \right) \right], \quad (\text{S17})$$

$$(\tilde{H}_F)_{12}^{K(\pi)} = (-1)^{(n_K+1)} \frac{3\gamma}{2(\eta^2 + 1)} \mathcal{J}_{2n_K-1}(\alpha f(r)) (k_x - i(-1)^{n_K \bmod 3} k_y) a_0 e^{2in_K m\phi}, \quad (\text{S18})$$

$$(\tilde{H}_F)_{22}^{K(\pi)} = \frac{\Omega}{2} - \frac{1}{\eta^2 + 1} \left[ \left\{ \left( n_K + \frac{1}{2} \right) \eta^2 + \left( n_K - \frac{1}{2} \right) \right\} \Omega + 6\gamma\eta \mathcal{J}_1(\alpha f(r)) \left( 1 - \frac{k^2 a_0^2}{4} \right) \right], \quad (\text{S19})$$

where  $\eta(r)$  is given by Eq. (S7). We have psuedo-OAM operators  $\hat{l}^{\Gamma(\pi)}$  and  $\hat{l}^{K(\pi)}$  given by

$$\hat{l}^{\Gamma(\pi)} = -i\partial_\phi + \left[ \frac{(2n_\Gamma - 1)}{2} m - (-1)^{n_\Gamma \bmod 3} \right], \quad (\text{S20})$$

$$\hat{l}^{K(\pi)} = -i\partial_\phi - \left( n_K m - \frac{(-1)^{n_K \bmod 3}}{2} \right). \quad (\text{S21})$$



Correspondingly, the eigenvalues of the pseudo-OAM operator are

$$l_{\pm}^{\Gamma(\pi)} = l \mp \left[ \frac{(2n_{\Gamma} - 1)}{2} m - (-1)^{n_{\Gamma} \bmod 3} \right], \quad (\text{S22})$$

$$l_{\pm}^{K(\pi)} = l \pm \left( n_K m - \frac{(-1)^{n_K \bmod 3}}{2} \right). \quad (\text{S23})$$

for  $\Gamma$  and  $K$  respectively. Thus, from the effective Hamiltonians we can see that there is a quadratic band crossing at  $\Gamma$  and linear band crossing at  $K$  point. The complete Floquet eigenstates for  $\Gamma$  and  $K$  are

$$\psi_l^{\Gamma(\pi)}(\mathbf{r}, t) = e^{i l_{\pm}^{\Gamma(\pi)} \phi} w_{\pm}^{\Gamma(\pi)}(r) u_{\pm}^{(1-n_{\Gamma})}(\Gamma, \mathbf{r}, t) + e^{i l_{\mp}^{\Gamma(\pi)} \phi} w_{\mp}^{\Gamma(\pi)}(r) u_{\mp}^{(n_{\Gamma})}(\Gamma, \mathbf{r}, t), \quad (\text{S24})$$

$$\psi_l^{K(\pi)}(\mathbf{r}, t) = e^{i l_{\pm}^{K(\pi)} \phi} w_{\pm}^{K(\pi)}(r) u_{\pm}^{(n_K)}(K, \mathbf{r}, t) + e^{i l_{\mp}^{K(\pi)} \phi} w_{\mp}^{K(\pi)}(r) u_{\mp}^{(-n_K)}(K, \mathbf{r}, t). \quad (\text{S25})$$

### ANALYTICAL RESULTS FOR DEGENERATE BOUND STATES

Consider a crossing between  $n_{\Gamma} = \pm 1$  modes at the Floquet zone center. We project the Floquet Hamiltonian onto the subspace of the degenerate Floquet modes and expand  $\mathbf{k}$  around the  $\Gamma$  point to obtain an effective Hamiltonian,

$$\tilde{H}_F^{\Gamma(0)} = \mu_{\Gamma}(r) \sigma_z + \frac{3\gamma}{2} \mathcal{F}_2(\alpha f(r)) a_0 [-i(k_x - ik_y) e^{-2im\phi} \sigma_+ + \text{h.c.}], \quad (\text{S26})$$

where the dynamically generated mass  $\mu_{\Gamma}(r) = -\Omega + 3\gamma \mathcal{F}_0(\alpha f(r))$  and  $\sigma_+ = (\sigma_x + i\sigma_y)/2$ . The mass term vanishes at  $r = r_c$  and changes sign on either side of the gap closing. The bound state solutions are found by solving the Schrodinger equation  $H_F^{\Gamma(0)} \chi_l(\mathbf{r}) = 0$  after replacing  $\mathbf{k}$  with  $-i\nabla_r$ . The radial wavefunctions  $w_{\pm}^{\Gamma(0)}(r)$  satisfy the differential equations,

$$\left[ \partial_r \mp \frac{(l \mp 1/2)}{r} + \frac{1}{2\mathcal{F}_2(\alpha f(r))} \partial_r \mathcal{F}_2(\alpha f(r)) \right] w_{\pm}^{\Gamma(0)} - \frac{2\mu_{\Gamma}(r)}{3\gamma \mathcal{F}_2(\alpha f(r)) a_0} w_{\mp}^{\Gamma(0)} = 0. \quad (\text{S27})$$

Above equation is in general difficult to solve analytically, although we still can get some information about the structure of  $w_{\pm}^{\Gamma(0)}(r)$  by looking at the limits  $r \rightarrow 0$  and  $r \rightarrow r_c$ . As  $r \rightarrow 0$ ,  $\mu_{\Gamma}(r) \rightarrow \text{constant}$  and  $\mathcal{F}_2(\alpha f(r)) \sim r^{2|m|}$  and Eq. (S27) becomes

$$r^{2|m|} \left[ \partial_r \mp \frac{(l \mp 1)}{r} \right] w_{\pm}^{\Gamma(0)} - c_0 w_{\mp}^{\Gamma(0)} = 0, \quad (\text{S28})$$

where  $c_0$  is a constant. Eq. (S28) can be equivalently written as

$$\left[ \partial_r^2 + \frac{2(|m| + 1)}{r} \partial_r - \frac{c_0^2}{r^{4|m|}} \right] w_{\pm}^{\Gamma(0)} = 0, \quad (\text{S29})$$

where we have also used the approximation that  $w_{\pm}^{\Gamma(0)}/r^2 \ll w_{\pm}^{\Gamma(0)}/r^{4|m|}$ . Eq. (S29) can be recast into the differential equation for the modified Bessel function after suitable substitutions, and thus we get

$$w_{\pm}^{\Gamma(0)}(r) \sim \frac{1}{r} \exp\left(-\frac{|c_0|}{(2|m| - 1)r^{2|m|-1}}\right). \quad (\text{S30})$$

From the form of the wavefunction we can see that as  $r \rightarrow 0$ ,  $w_{\pm}^{\Gamma(0)}(r) \rightarrow 0$  for all values of  $m$  as expected. As  $r \rightarrow r_c$ ,  $\mu_{\Gamma}(r) \sim (r_c - r)$  and  $\mathcal{F}_2(\alpha f(r)) \rightarrow \text{constant}$ . We perform the substitution  $w_{\pm}^{\Gamma(0)} = r^{\pm(l \mp 1/2)} v_{\pm}$  that transforms Eq.(S27) into

$$\left[ \partial_r^2 + \frac{1}{(r_c - r)} \partial_r - c_1^2 (r_c - r)^2 \right] v_{\pm} = 0, \quad (\text{S31})$$

where  $c_1$  is a constant and we have used the approximation  $|r - r_c| \ll r$  as  $r \rightarrow r_c$ . Thus we get the solutions as

$$w_{\pm}^{\Gamma(0)}(r) \sim r^{\pm(l \mp 1/2)} [A - B(r_c - r)^2 + c_1^2 (r_c - r)^4], \quad (\text{S32})$$

where  $A$  and  $B$  are arbitrary constants. The above solution is peaked around  $r = r_c$  and falls off on either side for all values of  $l$  and  $B > A$ .

Next we also consider a crossing between the  $n_K = 2, -3$  degenerate modes at the Floquet zone center. We expand  $\mathbf{k}$  around the  $K$  point and obtain the resulting effective Hamiltonian is given by

$$\tilde{H}_F^{K(0)} = \mu_K(r)\sigma_z + \frac{3}{2(\eta^2 + 1)}\gamma\mathcal{F}_4(\alpha f(r))a_0 [-i(k_x + ik_y)e^{5im\phi}\sigma_+ + \text{h.c.}], \quad (\text{S33})$$

where

$$\mu_K(r) = \left(\frac{3\eta^2 + 2}{\eta^2 + 1}\right)\Omega + \left(\frac{6\eta}{\eta^2 + 1}\right)\gamma\mathcal{F}_1(\alpha f(r)), \quad (\text{S34})$$

and  $\eta(r)$  given by Eq. (S7). In this case also, the mass term vanishes at  $r = r_c$  and changes sign on either side. The Floquet-Schrödinger at zero quasienergy results in the following differential equation for the bound state wavefunctions  $w_{\pm}^{K(0)}(r)$ ,

$$\left[\partial_r \pm \frac{(l \pm 1/2)}{r} + \frac{1}{2\mathcal{F}_4(\alpha f(r))}\partial_r \mathcal{F}_4(\alpha f(r))\right] w_{\pm}^{K(0)} - \frac{2(\eta^2 + 1)\mu_K(r)}{3\gamma\mathcal{F}_4(\alpha f(r))a_0} w_{\mp}^{K(0)} = 0. \quad (\text{S35})$$

Using similar arguments as before,

$$w_{\pm}^{K(0)}(r) \sim \begin{cases} \frac{1}{r} \exp\left[-\frac{|c'_0|}{(4|m|-1)r^{4|m|-1}}\right], & r \rightarrow 0 \\ r^{\pm(l\mp 1/2)}[A' - B'(r_c - r)^2 + c_1^2(r_c - r)^4], & r \rightarrow r_c \end{cases} \quad (\text{S36})$$

where  $c'_0, c'_1, A'$  and  $B'$  are constants and  $B' > A'$ . The spatial distribution of  $w_{\pm}^{K(0)}(r)$  is similar to that of  $w_{\pm}^{\Gamma(0)}(r)$ . Also the values of the constants  $c_0, c_1, c'_0$  and  $c'_1$  are fixed by the system parameters  $\Omega, \alpha, |m|$  and  $r_c$ .

## SELECTION RULES FOR $\Gamma \rightarrow K$ TRANSITION

### Floquet zone center

For the  $\Gamma \rightarrow K$  transition, we firstly need a scattering potential  $V(\mathbf{r})$  that connects  $\Gamma$  and  $K$ , since they are at different momenta. Then in order to have a non-zero overlap  $|\langle \psi_l^{K(0)} | V(\mathbf{r}) | \psi_l^{\Gamma(0)} \rangle|$ , we get appropriate conditions on  $n_{\Gamma}, n_K$  as well as OAM,  $m$ . Using Eqs. (S12) and (S13),

$$\begin{aligned} \langle \psi_l^{K(0)} | V(\mathbf{r}) | \psi_l^{\Gamma(0)} \rangle = & \int_0^{\infty} r dr \int_0^{2\pi} d\phi \int_0^{2\pi/\Omega} dt \left[ w_+^{\Gamma(0)} w_+^{K(0)} u_A^* e^{i(l_+^{\Gamma(0)} - l_+^{K(0)} - m)\phi} e^{-i(n_{\Gamma} + n_K + 1)\Omega t} \right. \\ & + w_-^{\Gamma(0)} w_+^{K(0)} u_A^* e^{i(l_-^{\Gamma(0)} - l_+^{K(0)} - m)\phi} e^{i(n_{\Gamma} - n_K - 1)\Omega t} \\ & + w_+^{\Gamma(0)} w_-^{K(0)} u_B^* e^{i(l_+^{\Gamma(0)} - l_-^{K(0)} - m)\phi} e^{-i(n_{\Gamma} - n_K)\Omega t} \\ & + w_-^{\Gamma(0)} w_-^{K(0)} u_B^* e^{i(l_-^{\Gamma(0)} - l_-^{K(0)} - m)\phi} e^{i(n_{\Gamma} + n_K)\Omega t} \\ & - w_+^{\Gamma(0)} w_+^{K(0)} u_B^* e^{i(l_+^{\Gamma(0)} - l_+^{K(0)})\phi} e^{-i(n_{\Gamma} + n_K)\Omega t} \\ & + w_-^{\Gamma(0)} w_+^{K(0)} u_B^* e^{i(l_-^{\Gamma(0)} - l_+^{K(0)})\phi} e^{i(n_{\Gamma} - n_K)\Omega t} \\ & - w_+^{\Gamma(0)} w_-^{K(0)} u_A^* e^{i(l_+^{\Gamma(0)} - l_-^{K(0)})\phi} e^{-i(n_{\Gamma} - n_K - 1)\Omega t} \\ & \left. + w_-^{\Gamma(0)} w_-^{K(0)} u_A^* e^{i(l_-^{\Gamma(0)} - l_-^{K(0)})\phi} e^{i(n_{\Gamma} + n_K + 1)\Omega t} \right]. \quad (\text{S37}) \end{aligned}$$

Since  $n_{\Gamma}, n_K > 0$ , we see that there are two possible cases for nonvanishing overlaps:  $n_{\Gamma} = n_K = 2 \pmod 3$  or  $n_{\Gamma} = n_K + 1 = 1 \pmod 3$ . In the former case, we must have either  $l_+^{\Gamma(0)} = l_-^{K(0)} + m$ , which yields  $m = 2$  and  $\langle \psi_l^{K(0)} | V(\mathbf{r}) | \psi_l^{\Gamma(0)} \rangle = \int_0^{\infty} w_+^{\Gamma(0)} w_-^{K(0)} u_B^* r dr$ , or  $l_-^{\Gamma(0)} = l_+^{K(0)}$ , which yields  $m = -2$  and  $\langle \psi_l^{K(0)} | V(\mathbf{r}) | \psi_l^{\Gamma(0)} \rangle = \int_0^{\infty} w_-^{\Gamma(0)} w_+^{K(0)} u_B^* r dr$ . Similarly, in the latter case, we must have either  $l_-^{\Gamma(0)} = l_+^{K(0)} + m$ , which yields  $m = 2$  and  $\langle \psi_l^{K(0)} | V(\mathbf{r}) | \psi_l^{\Gamma(0)} \rangle = \int_0^{\infty} w_-^{\Gamma(0)} w_+^{K(0)} u_A^* r dr$ , or  $l_+^{\Gamma(0)} = l_-^{K(0)}$ , which yields  $m = -2$  and  $\langle \psi_l^{K(0)} | V(\mathbf{r}) | \psi_l^{\Gamma(0)} \rangle = -\int_0^{\infty} w_+^{\Gamma(0)} w_-^{K(0)} u_A^* r dr$ .

### Floquet zone boundary

For  $\Omega/2$  quasienergy, we use Eqs. (S24) and (S25) to get a non-zero overlap

$$\begin{aligned}
\langle \psi_l^{K(\pi)} | V(\mathbf{r}) | \psi_l^{\Gamma(\pi)} \rangle = & \int_0^\infty r dr \int_0^{2\pi} d\phi \int_0^{2\pi/\Omega} dt \left[ w_+^{\Gamma(\pi)} w_+^{K(\pi)} u_A^* e^{i(l_+^{\Gamma(\pi)} - l_+^{K(\pi)} - m)\phi} e^{-i(n_\Gamma + n_K)\Omega t} \right. \\
& + w_-^{\Gamma(\pi)} w_+^{K(\pi)} u_A^* e^{i(l_-^{\Gamma(\pi)} - l_+^{K(\pi)} - m)\phi} e^{i(n_\Gamma - n_K - 1)\Omega t} \\
& + w_+^{\Gamma(\pi)} w_-^{K(\pi)} u_B^* e^{i(l_+^{\Gamma(\pi)} - l_-^{K(\pi)} - m)\phi} e^{-i(n_\Gamma - n_K)\Omega t} \\
& + w_-^{\Gamma(\pi)} w_-^{K(\pi)} u_B^* e^{i(l_-^{\Gamma(\pi)} - l_-^{K(\pi)} - m)\phi} e^{i(n_\Gamma + n_K - 1)\Omega t} \\
& - w_+^{\Gamma(\pi)} w_+^{K(\pi)} u_B^* e^{i(l_+^{\Gamma(\pi)} - l_+^{K(\pi)})\phi} e^{-i(n_\Gamma + n_K - 1)\Omega t} \\
& + w_-^{\Gamma(\pi)} w_+^{K(\pi)} u_B^* e^{i(l_-^{\Gamma(\pi)} - l_+^{K(\pi)})\phi} e^{i(n_\Gamma - n_K)\Omega t} \\
& - w_+^{\Gamma(\pi)} w_-^{K(\pi)} u_A^* e^{i(l_+^{\Gamma(\pi)} - l_-^{K(\pi)})\phi} e^{-i(n_\Gamma - n_K - 1)\Omega t} \\
& \left. + w_-^{\Gamma(\pi)} w_-^{K(\pi)} u_A^* e^{i(l_-^{\Gamma(\pi)} - l_-^{K(\pi)})\phi} e^{i(n_\Gamma + n_K)\Omega t} \right]. \tag{S38}
\end{aligned}$$

Since  $n_\Gamma, n_K > 0$ , we see that there are two possible cases for nonvanishing overlaps:  $n_\Gamma = n_K = 1 \pmod 3$  or  $n_\Gamma = n_K + 1 = 0 \pmod 3$ . In the former case we must have either  $l_+^{\Gamma(\pi)} = l_-^{K(\pi)} + m$ , which yields  $m = -1$  and  $\langle \psi_l^{K(\pi)} | V(\mathbf{r}) | \psi_l^{\Gamma(\pi)} \rangle = \int_0^\infty w_+^{\Gamma(\pi)} w_-^{K(\pi)} u_B^* r dr$  or  $l_-^{\Gamma(\pi)} = l_+^{K(\pi)}$ , which yields  $m = 1$  and  $\langle \psi_l^{K(\pi)} | V(\mathbf{r}) | \psi_l^{\Gamma(\pi)} \rangle = \int_0^\infty w_-^{\Gamma(\pi)} w_+^{K(\pi)} u_B^* r dr$ . Similarly, in the latter case, we must have either  $l_-^{\Gamma(\pi)} = l_+^{K(\pi)} + m$ , which yields  $m = -1$  and  $\langle \psi_l^{K(\pi)} | V(\mathbf{r}) | \psi_l^{\Gamma(\pi)} \rangle = \int_0^\infty w_-^{\Gamma(\pi)} w_+^{K(\pi)} u_A^* r dr$  or  $l_+^{\Gamma(\pi)} = l_-^{K(\pi)}$ , which yields  $m = 1$  and  $\langle \psi_l^{K(\pi)} | V(\mathbf{r}) | \psi_l^{\Gamma(\pi)} \rangle = -\int_0^\infty w_+^{\Gamma(\pi)} w_-^{K(\pi)} u_A^* r dr$ .

### $\Gamma \rightarrow K$ TRANSITION PROCESS

Let, the transition amplitudes be  $b = |\langle \psi_l^{K(\varepsilon)} | V(\mathbf{r}) | \psi_l^{\Gamma(\varepsilon)} \rangle|$  and  $b' = |\langle \psi_l^{K'(\varepsilon)} | V(\mathbf{r}) | \psi_l^{\Gamma(\varepsilon)} \rangle|$  where,  $\varepsilon = 0$  ( $m = \pm 2$ ) or  $\varepsilon = \Omega/2$  ( $m = \pm 1$ ). For a given quasienergy, the transition amplitudes are in general different and depend on the sign of OAM. The reason is that the potential  $V(\mathbf{r})$  connects the wavefunctions at opposite pairs of sublattices for  $\Gamma \rightarrow K$  and  $\Gamma \rightarrow K'$  for a particular sign of OAM. For example, consider the multifold degeneracy at the Floquet zone boundary with  $m = +1$  and  $n_\Gamma = n_K$ ,

$$b = \left| \int_0^\infty r dr w_-^{\Gamma(\pi)}(r) w_+^{K(\pi)}(r) u_B^* \right|, \tag{S39}$$

$$b' = \left| \int_0^\infty r dr w_+^{\Gamma(\pi)}(r) w_-^{K'(\pi)}(r) u_A^* \right|. \tag{S40}$$

Thus, OAM of light can distinguish between the  $K$  and  $K'$  points due to its non-trivial helicity. Then in the basis  $\{|\psi_l^{K(\varepsilon)}\rangle, |\psi_l^{\Gamma(\varepsilon)}\rangle, |\psi_l^{K'(\varepsilon)}\rangle\}$ ,  $V(\mathbf{r})$  can be written as,

$$V(\mathbf{r}) = \begin{pmatrix} 0 & b & 0 \\ b & 0 & b' \\ 0 & b' & 0 \end{pmatrix}. \tag{S41}$$

The eigenvalues are  $E = 0, \pm\sqrt{b^2 + b'^2}$  and the corresponding eigenvectors are,

$$\frac{1}{\sqrt{b^2 + b'^2}} \begin{pmatrix} b' \\ 0 \\ -b \end{pmatrix}, \quad \frac{1}{\sqrt{2(b^2 + b'^2)}} \begin{pmatrix} b \\ \pm\sqrt{b^2 + b'^2} \\ b' \end{pmatrix}.$$

So in the presence of  $V(\mathbf{r})$ , if we prepare our initial state at  $\Gamma$  as,  $|\Psi(t=0)\rangle = (0 \ 1 \ 0)^T$ , then after time  $t$ ,

$$|\Psi^{\Gamma \rightarrow K(K')}(t)\rangle = \frac{1}{\sqrt{b^2 + b'^2}} \begin{pmatrix} i \sin(\sqrt{b^2 + b'^2}t)b \\ \cos(\sqrt{b^2 + b'^2}t)\sqrt{b^2 + b'^2} \\ i \sin(\sqrt{b^2 + b'^2}t)b' \end{pmatrix}. \tag{S42}$$

Thus, when  $t = \frac{(2\nu+1)\pi}{2\sqrt{b^2+b'^2}}$  ( $\nu \in \mathbb{Z}$ ),  $|\Psi\rangle$  fully transitions into a superposition of  $K$  and  $K'$ , and when  $t = \frac{\nu\pi}{\sqrt{b^2+b'^2}}$ ,  $|\Psi\rangle$  transitions back to  $\Gamma$ . Similarly, if we start in a superposition of  $K$  and  $K'$ ,  $|\Psi(t=0)\rangle = (b \ 0 \ b')^T/\sqrt{b^2+b'^2}$ , then after time  $t$ ,

$$|\Psi^{K(K')\rightarrow\Gamma}(t)\rangle = \frac{1}{\sqrt{b^2+b'^2}} \begin{pmatrix} \cos(\sqrt{b^2+b'^2}t)b \\ i \sin(\sqrt{b^2+b'^2}t)\sqrt{b^2+b'^2} \\ \cos(\sqrt{b^2+b'^2}t)b' \end{pmatrix}. \quad (\text{S43})$$

Thus, when  $t = \frac{(2\nu+1)\pi}{2\sqrt{b^2+b'^2}}$  ( $\nu \in \mathbb{Z}$ ),  $|\Psi\rangle$  fully transitions into  $\Gamma$ , and when  $t = \frac{\nu\pi}{\sqrt{b^2+b'^2}}$ ,  $|\Psi\rangle$  transitions back to a superposition of  $K$  and  $K'$ . So even though we have used a three state basis, it is effectively a two-level system since  $K$  and  $K'$  points are at time-reversal invariant momenta. Therefore, using non-zero OAM and a suitable scattering potential  $V(\mathbf{r})$  we have engineered a method to create and manipulate superpositions of the multifold degenerate bound states at the  $\Gamma$  and  $K(K')$  points.